MDPI

Article

Shaping Micro-Bunched Electron Beams for Compact X-ray Free-Electron Lasers with Transverse Gradient Undulators

River R. Robles [1,2,*] and **James B. Rosenzweig** [3]

1 Department of Applied Physics, Stanford University, Stanford, CA 94035, USA
2 SLAC National Accelerator Laboratory, 2575 Sand Hill Rd, Menlo Park, CA 94025, USA
3 Department of Physics and Astronomy, University of California, Los Angeles, CA 90024, USA; rosen@physics.ucla.edu
* Correspondence: riverr@stanford.edu

Abstract: Laser-modulator-based micro-bunching of electron beams has been applied to many novel operating modes of X-ray free-electron lasers from harmonic generation to attosecond pulse production. Recently, it was also identified as a key enabling technology for the production of a compact XFEL driven by a relatively low-energy beam. In traditional laser modulator schemes with low-energy and high-current bunches, collective effects limit the possible working points that can be employed, and thus it is difficult to achieve optimal XFEL performance. We propose to utilize transverse longitudinal coupling in a transverse gradient undulator (TGU) to shape micro-bunched electron beams so as to optimize their performance in a compact X-ray free-electron laser. We show that a TGU added to a conventional laser modulator stage enables much more flexibility in the design, allowing one to generate longer micro-bunches less subject to slippage effects and even lower the slice emittance of the micro-bunches. We present a theoretical analysis of laser-based micro-bunching with an added TGU, simulation of compression with collective effects in such systems, and finally XFEL simulations demonstrating the gains in peak power enabled by the TGU. Although we focus on the application to compact XFELs, what we propose is a general phase space manipulation that may find utility in other applications as well.

Keywords: transverse gradient undulator; free-electron laser; eSASE; micro-bunching

1. Introduction

X-ray free-electron lasers (XFELs) have revolutionized the realm of ultra-fast, high-power X-ray science, producing X-ray pulses with a peak brightness that surpasses previous sources by nearly ten orders of magnitude [1–3]. The first XFEL capable of producing hard X-rays began operation in 2009: the Linac Coherent Light Source at SLAC National Accelerator Laboratory [4], followed by multiple additional XFEL facilities globally [5–9]. Though groundbreaking in terms of X-ray flux, these machines all share an accessibility issue. Due to their billion-dollar-class price tags and kilometer-scale footprints, there is an inherent difficulty in building new XFELs, which limits the number of scientific users that can be accommodated by the existing machines.

To address the accessibility issue, multiple concepts have been proposed to shorten and cheapen the XFEL [10–15]. Here, we focus on the Ultra-Compact X-ray Free-Electron Laser (UCXFEL) initiative [16]. The UCXFEL project is a UCLA-centered collaboration with the goal of producing an X-ray free-electron laser with a less than 40 m scale footprint and ~USD 40 million scale price tag. This ambitious design capitalizes on several recent developments in accelerator technology, most notably the demonstration of the ultra-high gradient operation of normal conducting, cryogenically cooled copper cavities [17], with demonstrated gradients in X-band accelerators approaching 250 MV/m. The higher gradient naturally shortens the accelerator complex. In addition to higher accelerating gradients,

large peak fields in these structures enable the production of ultra-high-brightness low-emittance beams in a cryogenically cooled photoinjector [18–20]. A lower-emittance beam allows for lasing to be performed with lower energy; in the UCXFEL case, it is just 1 GeV for soft X-rays [16].

Such high-brightness beams are only useful insofar as they can be propagated without degrading that brightness. Collective effects through beam acceleration and compression must be dealt with carefully, and the most dangerous effect in this context is emittance growth from coherent synchrotron radiation (CSR) during bunch compression. For that reason, the UCXFEL has been designed with a novel two-stage compression scheme. The second stage, in particular, compresses the beam into a train of high-current micro-bunches rather than compressing the bunch as a whole [21]. This scheme borrows from the concept of enhanced self-amplified spontaneous emission (eSASE), in which the beam energy is periodically modulated by interaction with an optical laser in a short wiggler [22,23]. This periodic modulation induces a large local chirp that can be compressed to high current with a relatively weak compressor chicane, thereby mitigating collective effects. A similar design has been proposed for a greater than 42 keV XFEL to study matter–radiation interactions at extremes [24,25].

Even with the eSASE compression scheme, the UCXFEL is still susceptible to collective effects. Compression to kA-scale current at just 1 GeV beam energy introduces notable perturbations in the longitudinal phase space. These perturbations can cause emittance growth in the transverse phase space in addition to limiting the achievable peak current. As discussed in the original UCXFEL proposal [16], in practice, these collective effects demand that designs move to larger eSASE modulation amplitudes, which, in addition to increasing the beam energy spread, also shortens the micro-bunches in the train for a fixed total compression factor [21,24]. Shorter micro-bunches can lead to gain degradation due to slippage, particularly in the soft X-ray regime, where compact XFELs are most immediately feasible.

In this paper, we propose to leverage transverse–longitudinal coupling to enhance the flexibility of eSASE compression schemes. Using the specific example of the transverse gradient undulator (TGU), we show that the diffuse spreading of the longitudinal coordinates due to transverse–longitudinal coupling can lengthen the micro-bunches and achieve the same ultimate peak current. Making use of transverse–longitudinal coupling provides an additional benefit: the particles that diffusively spread away from the peak of the current are those with large transverse action. Thus, the slice emittance at the center of the micro-bunches shrinks at the cost of the slice emittance outside of the current profile. This growth outside of the current spike is largely inconsequential, since those parts of the beam would not lase anyway due to their low local current. This scheme is trivially implemented at facilities utilizing eSASE micro-bunching: the simple addition of a TGU any time after the laser modulation has been performed can induce this effect.

The rest of this paper is structured as follows. In Section 2, we present theoretical analyses of both conventional eSASE compression and eSASE compression with an added TGU. We derive analytical formulas for the compression factor and slice-wise beam moments, which are useful for design studies and provide even more information than previously derived formulas for eSASE. Using these formulas, we study the limitations on slice emittance manipulation due to dispersion leaked out of the TGU. In Section 3, we perform simulation studies of the eSASE+TGU scheme within the context of the UCXFEL. First, we study compression in the presence of coherent synchrotron radiation, showing that TGU-based designs can help to mitigate emittance growth and longitudinal phase space distortion. We then perform simulations of lasing in the XFEL stage using both ideal beams and simulated beams, in both cases finding that the added micro-bunch length from the TGU transformation yields higher peak powers up to a factor of two.

2. Theoretical Approach

In this section, we present a theoretical analysis of micro-bunching schemes with a post-modulation transverse gradient undulator. We will begin by reviewing the theoretical framework of traditional eSASE compression before considering the added impact of a TGU. In what follows, we describe the beam using the coordinates $(x, x', y, y', s, \delta)$, where the first four are the transverse coordinates, s is the longitudinal coordinate along the bunch length, and δ is the relative energy offset of a particle relative to the average beam energy. Furthermore, we assume that the bunch length is much longer than the modulating laser wavelength λ_L. In this case, the dynamics can be treated as periodic in s with period λ_L, and so we will often instead work in the longitudinal coordinate $\theta = 2\pi s / \lambda_L$. Similarly, to make our analysis agnostic to the particular beam parameters, we will move to normalized coordinates $\chi = x / \sigma_x$, $\chi' = x' / \sigma_{x'}$, $v = y / \sigma_y$, $v' = y' / \sigma_{y'}$, and $p = \delta / \sigma_\delta$.

We are interested in understanding the phase space profiles that arise after laser modulation and compression, with the option of also considering a transverse–longitudinal coupling element such as the TGU. Of particular interest are the current and slice emittance, but also quantities like slice energy spread. Since we want to focus on slice-wise moments of the beam distribution within the micro-bunches, we introduce in Appendix A a formalism based on defining a moment-generating function (MGF) for the beam after the transformations. We summarize the results here for convenience. The MGF is defined as

$$M(\vec{t}, \theta) = \sum_{n=-\infty}^{\infty} b_n(\vec{t}) e^{in\theta} \tag{1}$$

where $\vec{t} = (t_x, t_{x'}, t_y, t_{y'}, t_\delta)$ and the b_n are the Fourier coefficients of the MGF, defined explicitly below. As we show in the Appendix A, moments of the distribution can be found by differentiating with respect to the appropriate element of the t vector, evaluating at $\vec{t} = \vec{0}$, and normalizing the result to $M(\vec{0}, \theta)$. For example, the slice-wise average offset in x is

$$\langle x \rangle(\theta) = \frac{1}{M(\vec{0}, \theta)} \frac{\partial M}{\partial t_x} \bigg|_{\vec{t} = \vec{0}} \tag{2}$$

and the slice-wise beam angle $\langle xx' \rangle(\theta)$ is

$$\langle xx' \rangle(\theta) = \frac{1}{M(\vec{0}, \theta)} \frac{\partial^2 M}{\partial t_x \partial t_{x'}} \bigg|_{\vec{t} = \vec{0}} \tag{3}$$

Finally, the current profile is simply the moment-generating function directly evaluated at $\vec{t} = \vec{0}$,

$$I(\theta) = M(\vec{0}, \theta) \tag{4}$$

We can call the function $b_n(\vec{t})$ the nth Fourier coefficient of the MGF. If a beam described by the initial distribution function $f_0(\vec{r}_0, \theta_0)$, where $\vec{r}_0 = (x_0, x'_0, y_0, y'_0, \delta_0)$, undergoes transformations that transform particle coordinates according to some mappings $\vec{r}(\vec{r}_0, \theta_0)$ and $\theta(\vec{r}_0, \theta_0)$, the Fourier coefficients of the MGF are

$$b_n(\vec{t}) = \frac{1}{2\pi} \int d\vec{r}_0 \int d\theta_0 e^{\vec{t} \cdot \vec{r}(\vec{r}_0, \theta_0) - in\theta(\vec{r}_0, \theta_0)} f_0(\vec{r}_0, \theta_0) \tag{5}$$

2.1. Analysis of Enhanced Self-Amplified Spontaneous Emission (eSASE)

The basic eSASE concept can be modeled as a two-part interaction, where first the beam energy is periodically modulated and second the modulated beam is compressed by a dispersive element such as a chicane. Modulation is achieved by resonant interaction of the laser and e-beam inside of a magnetic wiggler. In particular, the beam and laser interact resonantly if the wiggler wavenumber k_u, vector potential amplitude $K = eB_0 / k_u m_e c$, radiation wavenumber k_L, and average beam energy γ_0 satisfy the resonance condition

$$k_L = \frac{2\gamma_0^2 k_u}{1 + \frac{K^2}{2}} \tag{6}$$

The effect of the interaction is, in an ideal sense, a sinusoidal modulation of the energy. What matters for compression is the ratio of the modulation amplitude $\Delta\gamma$ to the uncorrelated energy spread of the beam σ_γ. In particular, we can describe the energy coordinate of a particular particle as $p_j = \frac{\gamma_j - \gamma_0}{\sigma_\gamma} \equiv \frac{\delta}{\sigma_\delta}$, where γ_j is the Lorentz factor of particle j and σ_γ is the uncorrelated energy spread in the beam. We can describe the longitudinal coordinate of a particle in the bunch as $\theta_j = k_L s_j$, where s_j is the longitudinal position of a particle relative to the bunch center. The action of the modulator is then summarized by

$$p_j \rightarrow p_j - A\sin(\theta_j) \tag{7}$$

where $A = \Delta\gamma / \sigma_\gamma$ is the modulation amplitude relative to the uncorrelated energy spread, and we have chosen a minus sign here for later convenience. This is followed by a compressor, which imposes a momentum compaction R_{56} with the effect

$$s_j \rightarrow s_j + R_{56}\frac{\gamma_j - \gamma_0}{\gamma_0} \tag{8}$$

which, in the language of our coordinates p_j and θ_j, is

$$\theta_j \rightarrow \theta_j + Bp_j \tag{9}$$

where we have defined $B = k_L R_{56} \sigma_\delta$. After this sequence of transformations, we can write the final p and θ in terms of the initial p_0 and θ_0 as

$$p(p_0, \theta_0) = p_0 - A\sin(\theta_0) \tag{10}$$
$$\theta(p_0, \theta_0) = \theta_0 + Bp_0 - AB\sin(\theta_0) \tag{11}$$

In Appendix A, we compute the Fourier coefficients of the MGF for eSASE. The result is

$$b_n(\vec{\tau}) = e^{\frac{1}{2}\left[\vec{\tau}_\perp^2 + (\tau_p - inB)^2\right]} J_n(A(nB + i\tau_p)) \tag{12}$$

where $\vec{\tau}_\perp = (\tau_\chi, \tau_{\chi'}, \tau_v, \tau_{v'})$ and $\vec{\tau}_\perp^2 \equiv \vec{\tau}_\perp \cdot \vec{\tau}_\perp$. We define $\vec{\tau}$ in the Appendix A as $\vec{t}$, with each coordinate normalized similarly to the particle coordinates (for example, $\tau_p = \sigma_\delta t_\delta$). In this case, since all of the dynamics are longitudinal, the most interesting outcome is the beam current profile, which can be written as

$$I(\theta) = I_0 \sum_{n=-\infty}^{\infty} e^{in\theta} J_n(nAB) e^{-\frac{1}{2}n^2 B^2} \tag{13}$$

where I_0 is the coasting beam current before the eSASE operations. We plot the compression at $\theta = 0$, $I(0)/I_0$, in Figure 1 for a representative range of A and B values. The curve along which the compression factor peaks corresponds roughly to full compression of the micro-bunch, with the region to the left of that indicating undercompression and to the right indicating overcompression.

In the UCXFEL design, the eSASE stage compresses the beam by a factor of 10 from a 400 A average current to 4 kA peak micro-bunched current. To make an explicit connection to the UCXFEL study, we can examine the characteristics of the contour along which a factor of 10 compression is achieved. Figure 2 shows the (A, B) contour yielding compression by a factor of 10 as well as the FWHM width of the resulting compressed micro-bunches. Below these two curves, we have plotted three characteristic compressed phase spaces with the projected current profile. The condition for fully compressing the modulation is $A = 1/B$, close to what is shown in the middle panel. To achieve $10\times$ compression and undercompress the micro-bunch, one has to increase the modulation amplitude, which leads

to a reduction in the micro-bunch FWHM. Going to an overcompressed working point, on the other hand, widens the micro-bunches significantly but only by introducing a bimodal slice energy distribution, which may not be ideal for FEL lasing. The overcompressed working point also requires a larger momentum compaction and could incur deleterious collective effects as a result, though higher energy XFEL designs are relatively robust to these collective effects and the bimodal slice energy distribution [24,25].
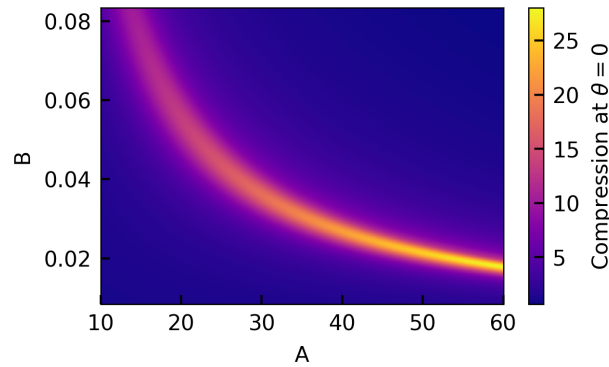

Figure 1. Compression factor at the center of the micro-bunch $\theta = 0$ as a function of A and B for eESASE compression.
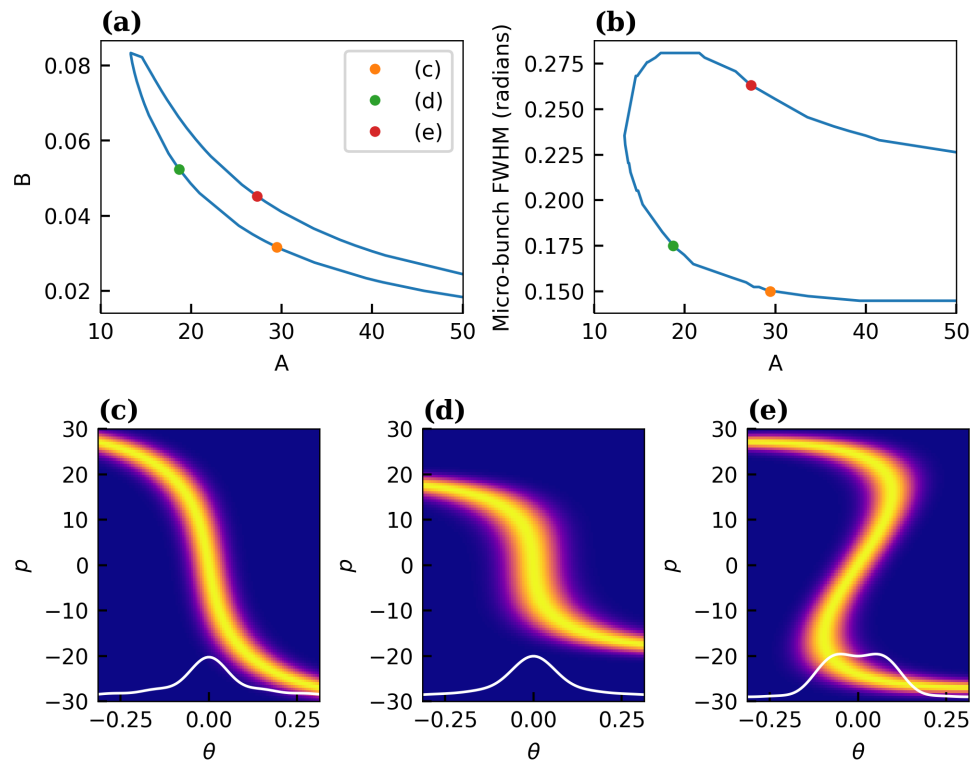

Figure 2. Characteristics of eSASE compression with a $10 \times$ compression factor. (**a**) The set of (A, B) values that yield $10 \times$ compression is plotted, highlighting three points whose corresponding micro-bunched phase spaces are shown in (**c**–**e**). (**b**) The full width at half maximum of the microbunches in units of the laser phase $\theta = k_L s$ is shown for the same (A, B) values as in (**a**), with the same points highlighted.

2.2. Analysis with an Added Transverse Gradient Undulator

In order to add a TGU to our analysis, we must first understand how a beam behaves as it propagates through a TGU. We first recall that a TGU is an undulator with transversely

canted poles, such that the normalized undulator strength K is a function of the transverse offset in the dispersive plane. We will assume the form $K(x) = K_0(1 + \alpha x)$. The motion of a particle in the presence of such a field was analyzed in [26], in which they found that the motion could be described using a linear transfer matrix **R** with the key non-trivial elements being

$$R_{16} = \frac{1}{\alpha}(1 - \cos(k_x L_{TGU})) \tag{14}$$

$$R_{26} = \frac{k_x}{\alpha} \sin(k_x L_{TGU}) \tag{15}$$

$$R_{51} = -R_{26} \tag{16}$$

$$R_{52} = -R_{16} \tag{17}$$

$$R_{56} = \frac{k_x^2 \eta_\alpha L_{TGU}}{\alpha} - \frac{k_x}{\alpha^2}(k_x L_{TGU} - \sin(k_x L_{TGU})) \tag{18}$$

where we have introduced $k_x = \alpha K_0 / \sqrt{2}\gamma_0$, $\eta_\alpha = (2 + K_0^2)/\alpha K_0^2$, and the length of the TGU L_{TGU}. While we could proceed with the analysis using the above equations, we will find it simpler to note that, for practical designs, it is often the case that $k_x L_{TGU} \ll 1$. As such, we may approximate the transfer matrix terms to first order in this parameter. This renders R_{16} and R_{52} negligible, so the transformation can be summarized as

$$x' \rightarrow x' + \frac{k_x^2 L_{TGU}}{\alpha}\delta \tag{19}$$

$$s \rightarrow s - \frac{k_x^2 L_{TGU}}{\alpha}(x - \eta_\alpha \delta) \tag{20}$$

Using the same longitudinal coordinates as in the eSASE case, but introducing $\chi = x/\sigma_x$ and $\chi' = x'/\sigma_{x'}$, we can write these rules as

$$\chi' \rightarrow \chi' + Gp \tag{21}$$

$$\theta \rightarrow \theta + T\chi + B_{TGU}p \tag{22}$$

where $G = \frac{\alpha K_0^2 L_{TGU}}{2\gamma_0^2} \frac{\sigma_\delta}{\sigma_{x'}}$, $T = -\frac{\alpha K_0^2 L_{TGU}}{2\gamma_0^2}\sigma_x k_L$, and $B_{TGU} = 2k_u L_{TGU}\sigma_\delta$. We note that T is equivalent to the T parameter defined in [27]. We see then that the TGU plays two roles. First, it shifts the phase θ proportional to the transverse offset of the beam in the canted plane. This will give rise to the dynamics that we are most interested in. The second effect is a deleterious one: the TGU leaves the beam with some non-vanishing dispersion, leading to a p-proportional kick to the transverse angle. This acts to increase the emittance of the beam, and must be taken into account and kept at an acceptable level. The phase-dispersing effect that we are interested in is quantified by the parameter T while the emittance diluting effect is quantified by G. In addition to these, the TGU has a momentum compaction given by a parameter B_{TGU}, which can be accounted for trivially by reducing the chicane B by the same amount.

Now we consider a three-part transformation in which an eSASE scheme is followed by a TGU. From the perspective of linear, single-particle beam dynamics, this is no different from placing the TGU between the modulation and compression stages, though the collective effects behave slightly differently between the two scenarios. Similarly to before, we can write the final particle coordinates in terms of the initial coordinates as

$$\chi_f = \chi_i \tag{23}$$

$$\chi'_f = \chi'_i + Gp_i - AG\sin(\theta_i) \tag{24}$$

$$p_f = p_i - A\sin(\theta_i) \tag{25}$$

$$\theta_f = \theta_i + Bp_i - AB\sin(\theta_i) + T\chi_i \tag{26}$$

where now technically B is the sum of the momentum compaction terms from the explicit compressor stage and from the TGU.

As before, we have provided a general analysis for the slice-wise beam moments in Appendix A. This results in the MGF Fourier coefficients:

$$b_n(\vec{\tau}) = \exp\left[\frac{1}{2}\left(\vec{\tau}_\perp^2 - n^2 T^2 - 2inT\tau_\chi + (-inB + \tau_p + G\tau_{\chi'})^2\right)\right] J_n\left(A(nB + i(\tau_p + G\tau_{\chi'}))\right) \tag{27}$$

which, as expected, reduces to Equation (12) when $G = T = 0$. We will again highlight the current profile, which can now be written

$$I(\theta) = I_0 \sum_{n=-\infty}^{\infty} e^{in\theta} J_n(nAB) e^{-\frac{1}{2}n^2(B^2 + T^2)} \tag{28}$$

Comparing this to the equivalent expression for pure eSASE compression, Equation (13), we see that an eSASE+TGU setup produces a current profile that is identical to an eSASE setup with effective eSASE parameters A_0 and B_0 defined by

$$A_0 = \frac{AB}{\sqrt{B^2 + T^2}} \tag{29}$$

$$B_0 = \sqrt{B^2 + T^2} \tag{30}$$

This suggests that if a design is forced, due to collective effects, to operate with a large modulation parameter A, then one can circumvent the subsequent micro-bunch shortening described in the previous section by adding a TGU to the beamline to diffusively spread the particles to an equivalent eSASE current profile with a longer micro-bunch length. We also note that although the current profiles are the same when this condition is met, the longitudinal phase space is not necessarily.

To elucidate the effect further, we show in Figure 3 the longitudinal phase space of one micro-bunch as it undergoes the eSASE+TGU transformations. The panels correspond to (a) the input beam, (b) after modulation, (c) after compression, and (d) after the TGU. The points in each plot are color-coded by the transverse position of the particle. We see as expected that, after compression (c), the micro-bunch is nearly fully compressed with no clear correlation between the longitudinal and transverse coordinates. Following the TGU (d), the particle phases are spread in correspondence with their transverse position such that a clear trend is visible and the central current spike has gotten longer. The case in Figure 3 is one in which we have chosen to match to an eSASE current profile with $A_0 = 16.5$ and $B_0 = 1/A_0$, which yields $10 \times$ compression, but using a TGU parameter $T = 0.95/A_0$. We note that if we choose to match to a certain pair of (A_0, B_0), only one of A, B, and T can be chosen independently. Having picked T, for example, B is set to $\sqrt{B_0^2 - T^2}$ and A is set to $A_0 B_0/B$.

Figure 3 implicitly reveals one additional interesting feature of the TGU transformation. The effect of the TGU is to push off-axis particles out of the central current spike, leaving those close to the axis in the region of highest current. As a result, the slice emittance in the central spike is reduced at the cost of increasing the slice emittance outside of the current spike. For emittance-dominated FEL designs, this could have beneficial effects for eventual lasing. We show this for the case in Figure 3 explicitly in Figure 4, where we plot the slice-wise compression factor and emittance relative to the initial emittance. In the middle of the current spike, the slice emittance has dropped to nearly half of its base value. We note that we have neglected the G parameter here, which is important as in practice it limits the emittance reduction effect.
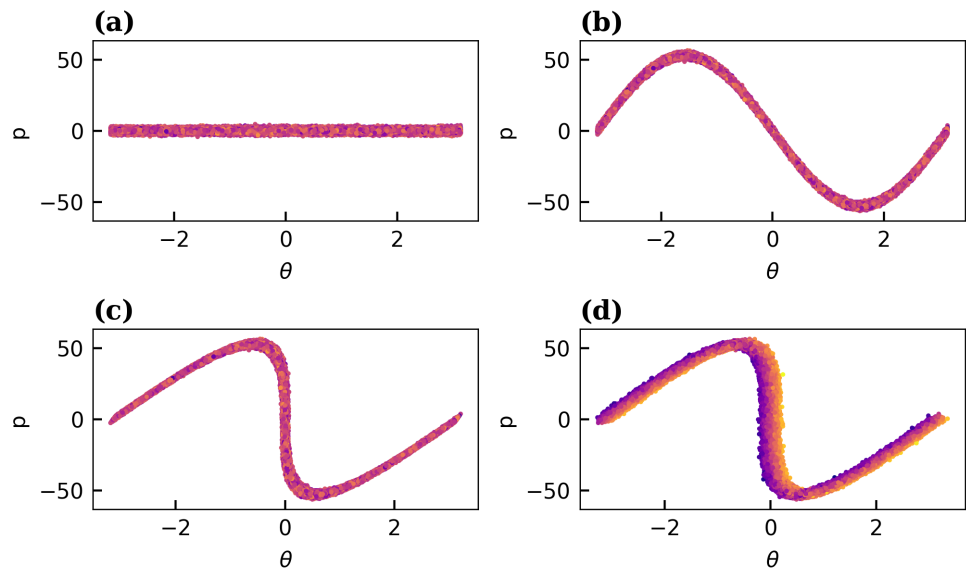
Figure 3. The longitudinal phase space of a single micro-bunch is shown during the eSASE+TGU process. The plots show the longitudinal phase space (**a**) at the input to the system, (**b**) after laser modulation, (**c**) after compression, and (**d**) after the TGU. This case has a modulation amplitude $A = 50$ matched to an eSASE parameter set $A_0 = 16.5$, $B_0 = 1/A_0$.
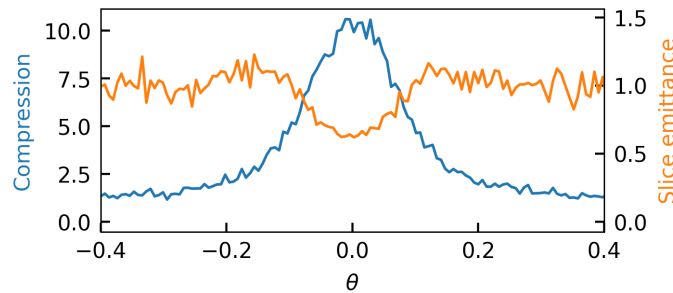

Figure 4. The compression factor and slice emittance are plotted for the beam at the end of Figure 3. We have neglected the dispersive term G for demonstration purposes.

We study the influence of the G parameter as well as the variation in slice emittance at the center of the spike with T in Figure 5. We again consider a case with the current profile matched to an eSASE current profile with $A_0 = 16.5$ and $B_0 = 1/A_0$. As we scan T, we fix A and B such that

$$A_0 = \frac{AB}{\sqrt{B^2 + T^2}} \tag{31}$$

$$B_0 = \sqrt{B^2 + T^2} \tag{32}$$

remain fixed. In panel (a), we plot the compression factor B as a function of T. In panel (b), we plot the slice emittance at the peak of the current spike as a function of T and the parameter G. The $G = 0$ part of the image is already interesting as it tells us that in order to see larger and larger reductions in slice emittance, we need to use larger T values. Of course, this implies larger modulation amplitudes as well, so we reduce the slice emittance at the cost of increasing the energy spread, which, for some designs, can be a beneficial tradeoff. As we then consider larger and larger G parameters, we see that the slice emittance begins to grow until it even surpasses the original emittance value. This highlights the tradeoff between emittance reduction from the phase spreading from T and emittance growth due to leaked dispersion from G. We note that this plot is for the particular case of $A_0 = 16.5$ and

$B_0 = 1/A_0$: for different working points at $10 \times$ compression and different compression values entirely, one will have different tradeoff curves. Finally, we note that T and G are related by nominally conserved scaling parameters:

$$\frac{|G|}{|T|} = \frac{\sigma_\delta}{\sigma_x \sigma_{x'} k_L} \simeq \frac{\sigma_\delta}{\epsilon_x k_L} = \frac{\sigma_\gamma}{\epsilon_{nx} k_L} \tag{33}$$

where we have defined the normalized emittance $\epsilon_{nx} = \gamma \sigma_x \sigma_{x'}$ assuming the beam to be approximately at the waist in the TGU, and the absolute slice energy spread $\sigma_\gamma = \gamma \sigma_\delta$. Given the value of $\sigma_\gamma / \epsilon_{nx} k_L$, one can draw a line with the corresponding slope in Figure 5, which tells how a particular design will behave with the TGU. For example, if $\sigma_\delta / \epsilon_{nx} k_L = 1$, Figure 5 shows that one can expect emittance reduction to $< 90\%$ if $T = 0.05$, but not much better than that. Furthermore, the fact that T and G are related by these conserved quantities tells us that the placement of the TGU relative to any acceleration between the modulator and the compressor does not impact the performance in terms of slice emittance dynamics. The particular scaling of $|G|/|T|$ tells us that the particles that are most susceptible to this slice emittance growth from G are those with low-emittance, large-energy-spread, and longer-wavelength eSASE modulations.
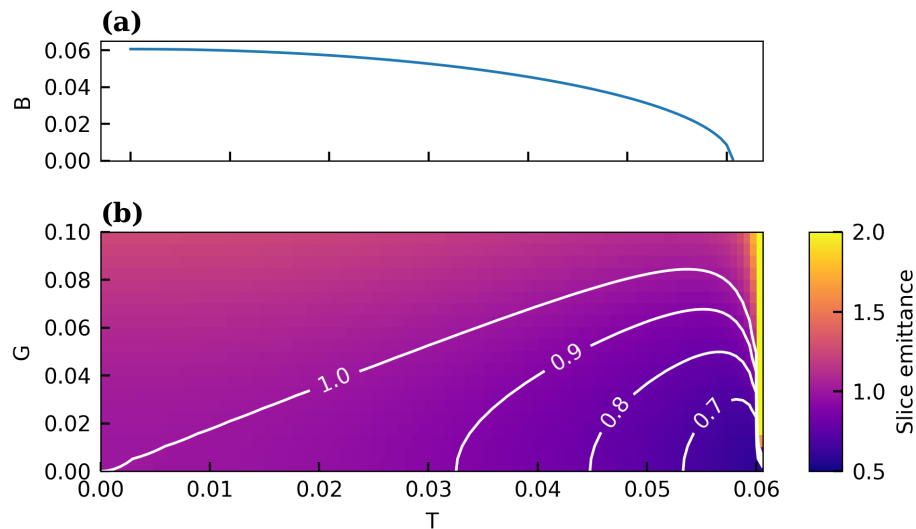

Figure 5. The impact of the dispersion term G is shown for an eSASE+TGU scheme designed to match an eSASE current profile with $A_0 = 16.5$ and $B_0 = 1/A_0$. (**a**) The value of B is shown as a function of T. (**b**) The slice emittance at the center of the micro-bunch relative to the initial slice emittance is plotted as a function of T and G, with white contour lines indicating values of 70%, 80%, 90%, and 100%. 1.0 is equal to the original slice emittance, thus indicating neither emittance growth nor reduction.

3. Application to UCXFEL

We now move on to simulations of a system inspired by UCXFEL-like parameters. We use a model system rather than the true start-to-end simulations of the UCXFEL in order to isolate the physics of the eSASE+TGU transformations. We will present both elegant [28] simulations of the upstream beamline and Genesis [29,30] simulations of the free-electron laser stage.

3.1. Elegant Simulations of Compression with and without the TGU

We begin with simulations of the electron beam dynamics. For this, we use the elegant code, which features a one-dimensional model of coherent synchrotron radiation (CSR) [28,31]. We are primarily interested in observing how the features induced by laser modulation and the TGU survive in the presence of these strong collective effects during compression, so to isolate the physics, we apply the laser modulation and TGU transfor-

mations using Equations (23)–(26), only using elegant code for the actual compression simulation. Our simulations begin with an ideal beam modeled off of the start-to-end UCXFEL beam. The average current is 400 A, with an uncorrelated slice energy spread of roughly 30 keV and a slice emittance of 50 nm rad. The final energy of the beam is 1 GeV, and the laser modulation is performed with a 10 μm wavelength. We will only simulate a 10 μm slice of the beam, which is valid because the CSR slippage length in one of the magnets for the nominal UCXFEL design is only $s_L \simeq \frac{R\theta^3}{24} \simeq 2.2$ μm [16,32], where R is the bending radius and θ is the bending angle. We will perform all simulations using 100k macroparticles within the 10 μm slice.

The first aspect of the dynamics that we would like to understand is: for a pure eSASE compression system, how do collective effects motivate the choice of modulation amplitude? For a fixed uncorrelated energy spread, a lower modulation amplitude implies a larger momentum compaction in the chicane and therefore stronger collective effects. Figure 6 illustrates this for three different modulation amplitudes: 16.5, 34, and 50. For each case, we scan the B parameter in the chicane (which we recall is proportional to the R_{56}), plotting the peak current as well as the projected and central slice normalized emittances. For the UCXFEL design, we desire to reach a 4 kA peak current, which we see becomes impossible with $A = 16.5$ due to CSR. In theory, one should get to 4 kA with $A = 16.5$ and $B = 1/A$, which is clearly not the case here. Increasing the modulation amplitude allows us to reach higher currents, as high as 6 kA with $A = 34$ or nearly 8 kA with $A = 50$; however, at these highest current working points, the slice and projected emittances both increase by more than a factor of two due to CSR. The sudden increase in emittance corresponds roughly with overcompression of the micro-bunch. Connecting back to the UCXFEL design study, in the two higher modulation amplitude cases, panels (b) and (c), we see that a 4 kA peak current is achieved for two values of B each. The lower value in each case corresponds to undercompression of the current spike—this entails relatively minimal emittance growth as we see in the figure, but with the cost of a reduced spike length as described by Figure 2. The higher B values that achieve a 4 kA peak current, on the other hand, correspond to overcompression. Although these overcompressed working points have a longer spike width per Figure 2, they also have a more than 100% emittance growth in both the slice and projected sense. For context, the UCXFEL design in [16] utilized the undercompressed 4 kA working point with $A = 34$ as a balance between micro-bunch width reduction and emittance growth. Ideally, we would stay undercompressed so as to minimize the emittance but maintain the longer micro-bunch width of the fully compressed and overcompressed working points.
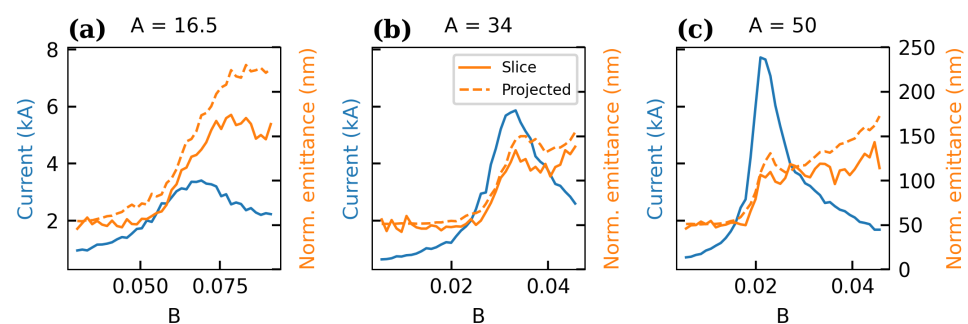

Figure 6. Elegant simulations of compression with a pure eSASE modulation. (**a**–**c**) all plot the peak current, projected normalized emittance, and central slice normalized emittance for three different modulation amplitudes as a function of the chicane B parameter.

With these tradeoffs in mind, let us now consider the addition of a TGU to the system, with the goal of simultaneously achieving long micro-bunch lengths and minimal emittance growth. We assume a modulation strength $A = 50$ and match the current profile to eSASE parameters $A_0 = 16.5$ and $B_0 = 1/A_0$. Figure 7 shows the longitudinal phase spaces,

current profiles, and slice emittance profiles for the $A = 34$, no TGU working point (top) and the $A = 50$, TGU working point (bottom). Several features are of note. The longitudinal phase space of the TGU working point is significantly less distorted than the no TGU working point due to reductions in the required chicane momentum compaction from both the TGU momentum compaction and the larger modulation amplitude. Similarly, we indeed see that the current profile is considerably wider with the TGU, increasing from 250 nm FWHM to 300 nm FWHM. Though this change sounds small, we will see in the next section that, for a slippage-dominated FEL even a 20% lengthening of the current spike can improve the peak power of the FEL by as much as a factor of two.

Focusing now on the slice emittance, we see that both cases reach a similar value near 75 nm rad. The TGU case is slightly lower, as is the increase in slice emittance on the edges of the current profile, which is consistent with our earlier analysis. For our case, $\sigma_\gamma / \epsilon_{nx} k_L \simeq 1.86$: a relatively large value due to the low emittance and long modulation wavelength. Due to the large modulation amplitude, T is roughly 0.057, leading to $G \simeq 0.1$. Looking back to Figure 5, we see that our design in fact incurs a bit of net emittance growth due to the TGU; however, it is balanced by the reduced CSR emittance growth.
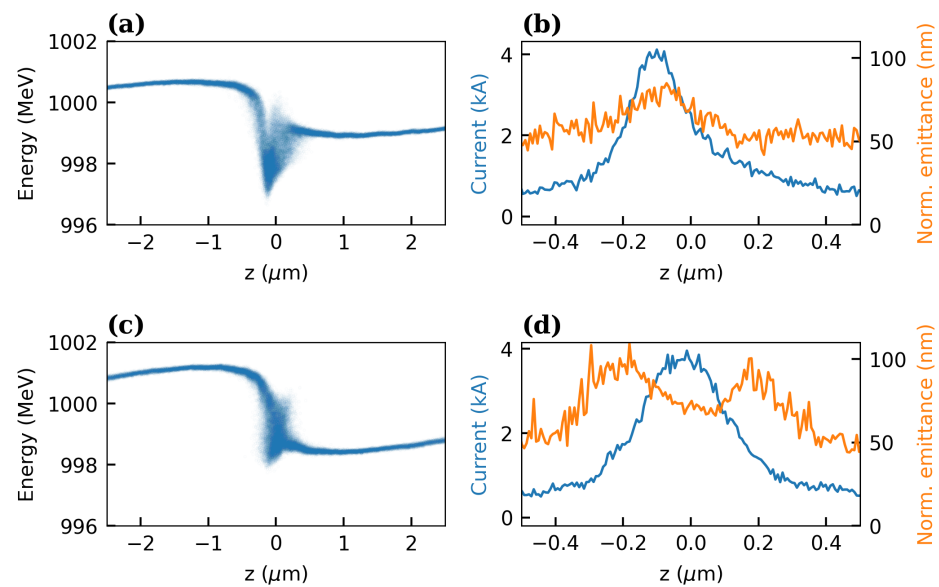

Figure 7. Elegant simulations of compression with and without a TGU. (**a**,**b**) are for a case with $A = 34$ and no TGU, while (**c**,**d**) are for a case with $A = 50$ and the use of a TGU to reproduce an eSASE current profile with $A_0 = 16.5$ and $B_0 = 1/A_0$. (**a**,**c**) are longitudinal phase spaces at the end of the compressor for one micro-bunch while (**b**,**d**) plot the current and slice emittance.

3.2. Genesis Simulations of FEL

We now move on to Genesis 1.3 simulations of the free-electron laser stage [29,30]. As before, the FEL parameters are motivated by the UCXFEL design study [16]. We attempt to lase 1 nm photons with a 6.5 mm period planar undulator with a total undulator length of 4 m. Again to focus on the TGU dynamics, we match the beam to a smooth focusing lattice in the undulator that maintains the core of the micro-bunches at a 5 μm transverse size. All simulations include macroscopic longitudinal space charge, implemented as a wake using the 1D formula from [33]. For each working point, we run either 32 or 64 statistically independent simulations starting from noise and report average results.

We begin with simulations using ideal beams, meaning beams generated simply by explicitly applying the transformations given in Equations (23)–(26). We again consider three modulation amplitudes: $A = 16.5$, $A = 34$, and $A = 50$. For the two higher modulation amplitudes, we additionally consider two different working points: one where the beam is directly compressed to 4 kA without a TGU and another where the beam is matched to the $A_0 = 16.5$, $B_0 = 1/A_0$ working point using the TGU. For each of the five

cases, we perform 32 statistically independent simulations. We plot the results in Figure 8. The left panel shows the peak power (averaged over the simulations) along the undulator length, and the right shows the average output power profile. The left panel shows that the XFEL output power suffers significantly in moving from $A = 16.5$ to the higher modulation amplitudes with no TGU. The peak power drops by nearly 50%. There is less of a shift in moving from $A = 34$ to $A = 50$, which is due to the plateau in micro-bunch FWHM for $A > 30$ observed in Figure 2, panel (b). Shifting to the TGU working points completely recovers that 50% of power, which reaffirms the claim that the drop in power originally is primarily due to slippage effects in the shortened micro-bunches. At first, it might be surprising that a 20% increase in bunch length can lead to a 50% increase in peak power; however, this can be explained by the exponential nature of FEL amplification. Increasing the micro-bunch length extends the FEL interaction by the undulator length corresponding to the amount of slippage in that added micro-bunch length. Thus, increasing the micro-bunch length by even one gain length worth of slippage can lead to a factor of e in output power. The total slippage in the 4-meter undulator is $N_u\lambda_r = 615$ nm, which is much longer than any of the micro-bunches in question. Thus, even a 20% increase in micro-bunch length gives large increases in peak power.
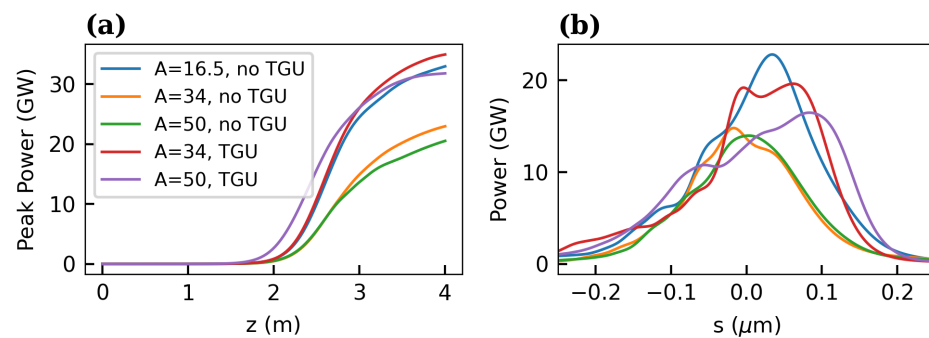

Figure 8. Results for Genesis simulations with ideal beams. (**a**) The peak power averaged over 32 independent simulations is plotted against undulator length for five different working points. (**b**) The average output power profile in the 32 simulations is plotted for the same five cases.

Next, we perform Genesis simulations of the two beams produced by elegant simulations in Figure 7. In this case, we performed 64 statistically independent simulations for each of the two working points and report average results. Again, both have relatively similar slice properties, with the exception of the longer micro-bunch width with the TGU. In this case, we see even more dramatic gains from the TGU, as shown in Figure 9. In this case, the peak power increases by nearly a factor of two from the $A = 34$, no TGU case to the $A = 50$, TGU case. As before, we attribute this large increase in power primarily to the increase in micro-bunch FWHM.
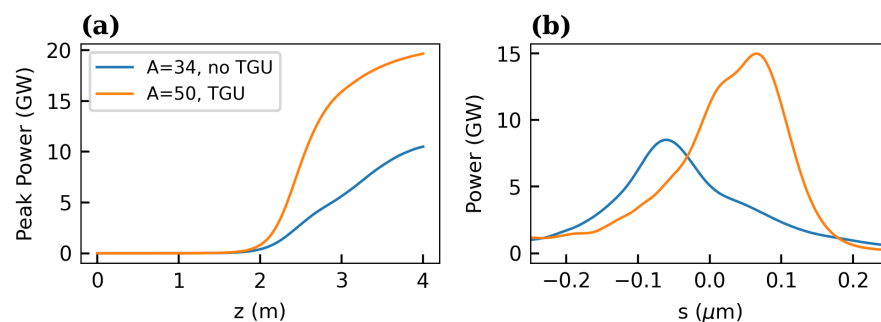

Figure 9. Results for Genesis simulations with elegant simulated beams. (**a**) The peak power averaged over 64 independent simulations is plotted along the undulator length. (**b**) The average output power profile is plotted for the two cases.

4. Conclusions

We have presented a simple extension to eSASE compression schemes that greatly enhances design flexibility. We have shown analytically that the addition of a TGU adds an additional tuning knob that allows one to produce flexible micro-bunch profiles regardless of the modulation amplitude that may be required by other machine constraints. Furthermore, we have shown that the transverse–longitudinal coupling nature of the TGU presents the possibility of reducing the slice emittance in the core of the micro-bunches, which can improve FEL lasing if the beam parameters allow it, i.e., if $\sigma_\gamma/\epsilon_{nx}k_L$ is sufficiently small. Furthermore, the simulation results show that the TGU is helpful in mitigating collective effects during compression, and that application to the UCXFEL system could promise peak power gains as high as a factor of two. The TGU is not the only mechanism by which to impose transverse–longitudinal coupling. Other methods may have unique advantages and disadvantages that are worth exploring. One particular example that is particularly relevant to eSASE is modulation by a laser that is closely matched in size to the electron beam, which induces a transversely dependent energy modulation amplitude. Finally, although we have focused on the UCXFEL in this paper, what we have presented is a general phase space manipulation technique that could find utility in any scheme involving micro-bunched electron beams.

Abbreviations

The following abbreviations are used in this manuscript:

XFEL	X-ray free-electron laser
UCXFEL	Ultra-Compact X-ray Free-Electron Laser
eSASE	enhanced self-amplified spontaneous emission
CSR	coherent synchrotron radiation
TGU	transverse gradient undulator
MGF	moment-generating function

Appendix A. Moment-Generating Function for Micro-Bunching Schemes

In this section, we present analytic formulas for analyzing the slice-wise properties of micro-bunched beams subject to arbitrary transfer matrices. We describe the beam using a probability density distribution $f(\vec{r}, \theta)$, where $\vec{r} = (x, x', y, y', \delta)$, and recall that a particular slice-wise moment of the beam is defined as an average over the distribution function:

$$\langle A(\vec{r}) \rangle(\theta) \equiv \frac{\int A(\vec{r}, \theta) f(\vec{r}, \theta) d\vec{r}}{\int f(\vec{r}, \theta) d\vec{r}} \tag{A1}$$

where $A(\vec{r})$ might be, for example, simply x if one were calculating the slice-wise centroid of the beam. For generating simple moments, meaning products of powers of the coordinates such as x, x^2, δx, etc., there is a powerful tool known as the moment-generating function (MGF):

$$M(\vec{t}, \theta) \equiv \int e^{\vec{t} \cdot \vec{r}} f(\vec{r}, \theta) d\vec{r} \tag{A2}$$

where $\vec{t} = (t_x, t_{x'}, t_y, t_{y'}, t_\delta)$. Generating the nth moment of a particular coordinate, say x, can be achieved by differentiating M with respect to t_x n times, evaluating at $\vec{t} = \vec{0}$, and dividing by the normalization factor $M(\vec{0}, \theta)$. A special case is the current distribution, which is just $M(\vec{0}, \theta)$. Thus, by providing a simple formula for M, we can derive any property of the beam we desire.

At this point, we can take advantage of the periodicity of our particular problem. Since we are dealing with periodically micro-bunched beams, we may expand the moment-generating function in a Fourier series:

$$M(\vec{t}, \theta) = \sum_n b_n(\vec{t}) e^{in\theta} \tag{A3}$$

where

$$b_n(\vec{t}) = \frac{1}{2\pi} \int d\vec{r} \int d\theta e^{\vec{t} \cdot \vec{r} - in\theta} f(\vec{r}, \theta) \tag{A4}$$

The evaluation of $b_n(\vec{t})$ can be greatly simplified by taking advantage of Liouville's theorem. As in [34], we can note here that since the phase space area is conserved, the probability $f(\vec{r}, \theta) d\vec{r} d\theta$ is the same no matter where we evaluate it in the beamline. It is simplest to evaluate it at the entrance to the laser modulator in this case, where the beam has some distribution $f_0(\vec{r}_0, \theta_0)$. With this, we can write

$$b_n(\vec{t}) = \frac{1}{2\pi} \int d\vec{r}_0 \int d\theta_0 e^{\vec{t} \cdot \vec{r}(\vec{r}_0, \theta_0) - in\theta(\vec{r}_0, \theta_0)} f_0(\vec{r}_0, \theta_0) \tag{A5}$$

where now we have expressed $\vec{r}$ and θ in the exponent in terms of their values at the initial position. From here on, we will restrict our attention to beams that begin as an uncorrelated Gaussian in the transverse and energy variables and effectively infinite flat-tops in the longitudinal coordinate:

$$f_0(\vec{r}_0, \theta_0) = \frac{1}{(2\pi)^{5/2} \epsilon_x \epsilon_y \sigma_\delta} \exp\left[-\frac{x^2}{2\sigma_x^2} - \frac{x'^2}{2\sigma_{x'}^2} - \frac{y^2}{2\sigma_y^2} - \frac{y'^2}{2\sigma_{y'}^2} - \frac{\delta^2}{2\sigma_\delta^2} \right] \tag{A6}$$

One last step that we can take is to put these expressions into the normalized forms that we used earlier in the text. Defining $\vec{\rho} \equiv (\chi, \chi', \upsilon, \upsilon', p) = \left(\frac{x}{\sigma_x}, \frac{x'}{\sigma_{x'}}, \frac{y}{\sigma_y}, \frac{y'}{\sigma_{y'}}, \frac{\delta}{\sigma_\delta} \right)$, we have

$$b_n(\vec{\tau}) = \frac{1}{2\pi} \int d\vec{\rho}_0 \int d\theta e^{\vec{\tau} \cdot \vec{\rho}(\vec{\rho}_0, \theta_0) - in\theta(\vec{\rho}_0, \theta_0)} F_0(\vec{\rho}_0, \theta_0) \tag{A7}$$

where now $\vec{\tau} \equiv (\tau_\chi, \tau_{\chi'}, \tau_\upsilon, \tau_{\upsilon'}, \tau_p) = (\sigma_x t_x, \sigma_{x'} t_{x'}, \sigma_y t_y, \sigma_{y'} t_{y'}, \sigma_\delta t_\delta)$ and $F_0(\vec{R}_0, \theta_0) = \frac{1}{(2\pi)^{5/2}} e^{-\frac{|\vec{R}_0|^2}{2}}$. This is as far as we can go without specifying the transformation rules from $\vec{r}_0$ and θ_0 to $\vec{r}$ and θ. We will now evaluate the Fourier coefficients of the moment-generating function for the specific cases of eSASE and eSASE with a TGU.

Appendix A.1. Formulas for eSASE

Recall that the transformations for eSASE were

$$p(p_0, \theta_0) = p_0 - A\sin(\theta_0) \tag{A8}$$
$$\theta(p_0, \theta_0) = \theta_0 + Bp_0 - AB\sin(\theta_0) \tag{A9}$$

Therefore,

$$b_n(\vec{\tau}) = \frac{e^{\frac{1}{2}\vec{\tau}_\perp^2}}{(2\pi)^{3/2}} \int dp_0 \exp\left[p_0(\tau_p - inB) - \frac{p_0^2}{2}\right] \int d\theta_0 \exp\left[-in\theta_0 - A(\tau_p - inB)\sin(\theta_0)\right] \tag{A10}$$

Notice that since the transformations depend only on the longitudinal coordinates, the transverse coordinates give the trivial term $e^{\frac{\vec{\tau}_\perp^2}{2}}$, where $\vec{\tau}_\perp$ consists of the four transverse components of $\vec{\tau}$. The p_0 integral can be taken easily. The θ_0 integral can be evaluated by utilizing the Jacobi–Anger expansion

$$e^{iz\sin(\theta)} = \sum_{k=-\infty}^{\infty} J_k(z)e^{ik\theta} \tag{A11}$$

This results in

$$b_n(\vec{\tau}) = \frac{e^{\frac{1}{2}\vec{\tau}_\perp^2}}{2\pi} e^{\frac{1}{2}(\tau_p - iBn)^2} \int d\theta_0 e^{-in\theta_0} \sum_k e^{ik\theta_0} J_k\left(A(nB + i\tau_p)\right) \tag{A12}$$

where now finally we utilize the definition of the delta function $\delta(x) = \frac{1}{2\pi}\int \frac{dk}{2\pi}e^{ikx}$ to write

$$b_n(\vec{\tau}) = e^{\frac{1}{2}\vec{\tau}_\perp^2} e^{\frac{1}{2}(\tau_p - inB)^2} J_n\left(A(nB + i\tau_p)\right) \tag{A13}$$

The Fourier coefficients relevant to computing the micro-bunched current profile come from evaluating at $\vec{\tau} = \vec{0}$:

$$b_n(\vec{0}) = e^{-\frac{1}{2}n^2B^2} J_n(nAB) \tag{A14}$$

Indeed, this is as is usually shown in the literature [27,35].

Appendix A.2. Formulas for eSASE with TGU

We now repeat the process of the previous section using the formulas appropriate for the scheme including a TGU:

$$\chi(\chi_0, \chi_0', p_0, \theta_0) = \chi_0 \tag{A15}$$
$$\chi'(\chi_0, \chi_0', p_0, \theta_0) = \chi_0' + Gp_0 - AG\sin(\theta_0) \tag{A16}$$
$$p(\chi_0, \chi_0', p_0, \theta_0) = p_0 - A\sin(\theta_0) \tag{A17}$$
$$\theta(\chi_0, \chi_0', p_0, \theta_0) = \theta_0 + Bp_0 - AB\sin(\theta_0) + T\chi_0 \tag{A18}$$

It is straightforward to evaluate the resulting integrals to determine the Fourier coefficients of the moment-generating function, using again the Jacobi–Anger expansion and the definition of the delta function. The result is

$$b_n(\vec{\tau}) = \exp\left[\frac{1}{2}\left(\vec{\tau}_\perp^2 - n^2T^2 - 2inT\tau_\chi + (-inB + \tau_p + G\tau_{\chi'})^2\right)\right] J_n\left(A(nB + i(\tau_p + G\tau_{\chi'}))\right) \tag{A19}$$

And again it is useful to quote the particular Fourier coefficient relevant for the current:

$$b_n(\vec{0}) = e^{-\frac{1}{2}n^2(B^2+T^2)} J_n(nAB) \tag{A20}$$

References

1. McNeil, B.W.; Thompson, N.R. X-ray free-electron lasers. *Nat. Photonics* **2010**, *4*, 814–821. [CrossRef]
2. Huang, Z.; Kim, K.J. Review of X-ray free-electron laser theory. *Phys. Rev. Spec. Top.-Accel. Beams* **2007**, *10*, 034801. [CrossRef]
3. Pellegrini, C.; Marinelli, A.; Reiche, S. The physics of X-ray free-electron lasers. *Rev. Mod. Phys.* **2016**, *88*, 015006. [CrossRef]
4. Emma, P.; Akre, R.; Arthur, J.; Bionta, R.; Bostedt, C.; Bozek, J.; Brachmann, A.; Bucksbaum, P.; Coffee, R.; Decker, F.J.; et al. First lasing and operation of an ångstrom-wavelength free-electron laser. *Nat. Photonics* **2010**, *4*, 641–647. [CrossRef]

5. Altarelli, M.; Brinkmann, R.; Chergui, M.; Decking, W.; Dobson, B.; Düsterer, S.; Grübel, G.; Graeff, W.; Graafsma, H.; Hajdu, J.; et al. The European X-ray Free-Electron Laser. Technical Design Report. Available online: https://bib-pubdb1.desy.de/record/77248/files/european-xfel-tdr.pdf (accessed on 31 August 2023).

6. Ishikawa, T.; Aoyagi, H.; Asaka, T.; Asano, Y.; Azumi, N.; Bizen, T.; Ego, H.; Fukami, K.; Fukui, T.; Furukawa, Y.; et al. A compact X-ray free-electron laser emitting in the sub-ångström region. *Nat. Photonics* **2012**, *6*, 540–544. [CrossRef]

7. Ko, I.S.; Kang, H.S.; Heo, H.; Kim, C.; Kim, G.; Min, C.K.; Yang, H.; Baek, S.Y.; Choi, H.J.; Mun, G.; et al. Construction and commissioning of PAL-XFEL facility. *Appl. Sci.* **2017**, *7*, 479. [CrossRef]

8. Milne, C.J.; Schietinger, T.; Aiba, M.; Alarcon, A.; Alex, J.; Anghel, A.; Arsov, V.; Beard, C.; Beaud, P.; Bettoni, S.; et al. SwissFEL: The Swiss X-ray free electron laser. *Appl. Sci.* **2017**, *7*, 720. [CrossRef]

9. Prat, E.; Al Haddad, A.; Arrell, C.; Augustin, S.; Boll, M.; Bostedt, C.; Calvi, M.; Cavalieri, A.L.; Craievich, P.; Dax, A.; et al. An X-ray free-electron laser with a highly configurable undulator and integrated chicanes for tailored pulse properties. *Nat. Commun.* **2023**, *14*, 5069. [CrossRef]

10. Wang, W.; Feng, K.; Ke, L.; Yu, C.; Xu, Y.; Qi, R.; Chen, Y.; Qin, Z.; Zhang, Z.; Fang, M.; et al. Free-electron lasing at 27 nanometres based on a laser wakefield accelerator. *Nature* **2021**, *595*, 516–520. [CrossRef]

11. Pompili, R.; Alesini, D.; Anania, M.; Arjmand, S.; Behtouei, M.; Bellaveglia, M.; Biagioni, A.; Buonomo, B.; Cardelli, F.; Carpanese, M.; et al. Free-electron lasing with compact beam-driven plasma wakefield accelerator. *Nature* **2022**, *605*, 659–662. [CrossRef]

12. Habib, A.; Manahan, G.; Scherkl, P.; Heinemann, T.; Sutherland, A.; Altuiri, R.; Alotaibi, B.; Litos, M.; Cary, J.; Raubenheimer, T.; et al. Attosecond-Angstrom free-electron-laser towards the cold beam limit. *Nat. Commun.* **2023**, *14*, 1054. [CrossRef] [PubMed]

13. Graves, W.; Kärtner, F.; Moncton, D.; Piot, P. Intense superradiant x rays from a compact source using a nanocathode array and emittance exchange. *Phys. Rev. Lett.* **2012**, *108*, 263904. [CrossRef] [PubMed]

14. Graves, W.; Bessuille, J.; Brown, P.; Carbajo, S.; Dolgashev, V.; Hong, K.H.; Ihloff, E.; Khaykovich, B.; Lin, H.; Murari, K.; et al. Compact X-ray source based on burst-mode inverse Compton scattering at 100 kHz. *Phys. Rev. Spec. Top.-Accel. Beams* **2014**, *17*, 120701. [CrossRef]

15. Nanni, E.; Graves, W.; Moncton, D. Nanomodulated electron beams via electron diffraction and emittance exchange for coherent X-ray generation. *Phys. Rev. Accel. Beams* **2018**, *21*, 014401. [CrossRef]

16. Rosenzweig, J.; Majernik, N.; Robles, R.; Andonian, G.; Camacho, O.; Fukasawa, A.; Kogar, A.; Lawler, G.; Miao, J.; Musumeci, P.; et al. An ultra-compact X-ray free-electron laser. *New J. Phys.* **2020**, *22*, 093067. [CrossRef]

17. Cahill, A.; Rosenzweig, J.; Dolgashev, V.A.; Tantawi, S.G.; Weathersby, S. High gradient experiments with X-band cryogenic copper accelerating cavities. *Phys. Rev. Accel. Beams* **2018**, *21*, 102002. [CrossRef]

18. Rosenzweig, J.B.; Cahill, A.; Carlsten, B.; Castorina, G.; Croia, M.; Emma, C.; Fukusawa, A.; Spataro, B.; Alesini, D.; Dolgashev, V.; et al. Ultra-high brightness electron beams from very-high field cryogenic radiofrequency photocathode sources. *Nucl. Instruments Methods Phys. Res. Sect. A Accel. Spectrometers Detect. Assoc. Equip.* **2018**, *909*, 224–228. [CrossRef]

19. Rosenzweig, J.; Cahill, A.; Dolgashev, V.; Emma, C.; Fukasawa, A.; Li, R.; Limborg, C.; Maxson, J.; Musumeci, P.; Nause, A.; et al. Next generation high brightness electron beams from ultrahigh field cryogenic rf photocathode sources. *Phys. Rev. Accel. Beams* **2019**, *22*, 023403. [CrossRef]

20. Robles, R.R.; Camacho, O.; Fukasawa, A.; Majernik, N.; Rosenzweig, J.B. Versatile, high brightness, cryogenic photoinjector electron source. *Phys. Rev. Accel. Beams* **2021**, *24*, 063401. [CrossRef]

21. Robles, R.; Rosenzweig, J. Compression of ultra-high brightness beams for a compact X-ray free-electron laser. *Instruments* **2019**, *3*, 53. [CrossRef]

22. Zholents, A.A.; Fawley, W.M.; Emma, P.; Huang, Z.; Reiche, S.; Stupakov, G. *Current-Enhanced SASE Using an Optical Laser and Its Applicationto the LCLS*; Technical Report; Lawrence Berkeley National Lab. (LBNL): Berkeley, CA, USA, 2004.

23. Zholents, A.A. Method of an enhanced self-amplified spontaneous emission for X-ray free electron lasers. *Phys. Rev. Spec. Top.-Accel. Beams* **2005**, *8*, 040701. [CrossRef]

24. Carlsten, B.E.; Anisimov, P.M.; Barnes, C.W.; Marksteiner, Q.R.; Robles, R.R.; Yampolsky, N. High-brightness beam technology development for a future dynamic mesoscale materials science capability. *Instruments* **2019**, *3*, 52. [CrossRef]

25. Xu, H.; Anisimov, P.M.; Carlsten, B.E.; Duffy, L.D.; Marksteiner, Q.R.; Robles, R.R. X-ray Free Electron Laser Accelerator Lattice Design Using Laser-Assisted Bunch Compression. *Appl. Sci.* **2023**, *13*, 2285. [CrossRef]

26. Liu, T.; Huang, Z.; Qin, W.; Ding, Y.; Wang, D. Beam Dynamics Studies of the Transverse Gradient Undulator and Its Application to Suppression of Microbunching Instability. In Proceedings of the IPAC2017, Copenhagen, Denmark, 14–19 May 2017.

27. Feng, C.; Deng, H.; Wang, D.; Zhao, Z. Phase-merging enhanced harmonic generation free-electron laser. *New J. Phys.* **2014**, *16*, 043021. [CrossRef]

28. Borland, M. Elegant: A Flexible SDDS-Compliant Code for Accelerator Simulation. Available online: https://www.osti.gov/biblio/761286 (accessed on 20 August 2023).

29. Reiche, S. GENESIS 1.3: A fully 3D time-dependent FEL simulation code. *Nucl. Instruments Methods Phys. Res. Sect. A Accel. Spectrometers Detect. Assoc. Equip.* **1999**, *429*, 243–248. [CrossRef]

30. Reiche, S. Genesis-1.3-Version4. 2022. Available online: https://github.com/svenreiche/Genesis-1.3-Version4 (accessed on 20 August 2023).

31. Borland, M. Simple method for particle tracking with coherent synchrotron radiation. *Phys. Rev. Spec. Top.-Accel. Beams* **2001**, *4*, 070701. [CrossRef]

32.   Saldin, E.L.; Schneidmiller, E.A.; Yurkov, M. On the coherent radiation of an electron bunch moving in an arc of a circle. *Nucl. Instruments Methods Phys. Res. Sect. A Accel. Spectrometers Detect. Assoc. Equip.* **1997**, *398*, 373–394. [CrossRef]
33.   Ding, Y.; Huang, Z.; Ratner, D.; Bucksbaum, P.; Merdji, H. Generation of attosecond X-ray pulses with a multicycle two-color enhanced self-amplified spontaneous emission scheme. *Phys. Rev. Spec. Top.-Accel. Beams* **2009**, *12*, 060703. [CrossRef]
34.   Xiang, D.; Stupakov, G. Echo-enabled harmonic generation free electron laser. *Phys. Rev. Spec. Top.-Accel. Beams* **2009**, *12*, 030702. [CrossRef]
35.   Hemsing, E.; Stupakov, G.; Xiang, D.; Zholents, A. Beam by design: Laser manipulation of electrons in modern accelerators. *Rev. Mod. Phys.* **2014**, *86*, 897. [CrossRef]